International Conference on Space Optics—ICSO 2024
Antibes Juan-les-Pins, France
21-25 October 2024

Edited by Philippe Kubik, Frédéric Bernard, Kyriaki Minoglou and Nikos Karafolas

Tundra satellite orbits for very high-throughput optical feederlinks – Part II: system characteristics and trade-offs

International Conference on Space Optics — ICSO 2024, edited by Frédéric Bernard, Nikos Karafolas, Philippe Kubik, Kyriaki Minoglou, Proc. of SPIE Vol. 13699, 136996D · © 2025 ESA and CNES · 0277-786X · doi: 10.1117/12.3075360

Tundra satellite orbits for very high-throughput optical feederlinks – Part II: system characteristics and trade-offs

Sander Orbons[a], Thomas Dreischer[b], Rudolf Saathof*[a], Stijn Mast[c], and Thai-Chien Buy[b]
[a]Delft University of Technology, Kluyverweg 1, Delft, The Netherlands [b]Airbus Netherlands B.V., Mendelweg 30, Leiden, The Netherlands [c]Optoelectronics Section, European Space Agency, Keplerlaan 1, Noordwijk, The Netherlands

ABSTRACT

Future Very High-Throughput Satellites are foreseen to implement optical ground-to-satellite feeder links to achieve multi-terabit-per-second data rates. Optical links, however, are highly susceptible to atmospheric losses caused by turbulence, absorption, and scattering, especially at low elevation angles. Despite prior confirmation of cloud-free network availability, high-latitude stations have been notably absent from optical feeder link studies due to the limitation of Geostationary orbits in providing sufficiently high link elevation angles. Tundra orbits present a promising alternative to Geostationary orbits, because they can ensure continuous coverage also at high-latitude regions like in Europe and Canada, with link geometries highly suitable for optical communications. Tundra link architectures require two satellites for constant coverage, but they deliver at least twice the data volume throughput from the same ground network which balances. This paper addresses optical feeder link implementation aspects in Tundra orbits and selects a suitable orbit to service Canada while considering aspects such as coverage, radiation environment, pointing angles, and delta-v impact. A complementary paper, Part I, deals with end-to-end communications simulations while this paper focusses on uplink amplitude statistics and related dynamic turbulence penalties that are considered a major design driver in optical feederlink architectures. The analysis in this paper focuses on angular anisoplanatism and highlights the link geometry impact on pre-compensation efficacy. This analysis anticipates a 3.6 dB link budget advantage for a two-satellite Tundra configuration over Geostationary under benign atmospheric conditions, using the same ground network. Which leads to a more than twice the data throughput and balances using two satellites instead of one. These findings highlight Tundra constellations' potential to enhance satellite communication infrastructure, providing robust, efficient service in regions where Geostationary orbits faces limitations.

Keywords: VHTS Satellites, Optical Feeder Links, Tundra Orbits, Geostationary Orbits, Anisoplanatism, Delta-v

1. INTRODUCTION

1.1 Very high-throughput satellites and optical feeder links

Continuing demand for capacity growth and cost reduction in satellite communication drive the development of Very High-Throughput Satellites (VHTS) with terabit-per-second (Tb/s) data rates. Optical Feeder Links (OFL) are considered a crucial technological development to effectively achieve up- and downlink data rates of this magnitude. Free-space optical links provide license free-spectrum with data rates in the order of terahertz per ground station, releasing coveted RF-frequency spectrum for exclusive use on user-links [1]. Furthermore, the highly directive optical beams potentially lower SWaP requirements and increase the difficulty for third parties to intercept the communication beam. Site diversity is considered to ensure cloud-free line-of-sight visibility with 5-14 Optical Ground Stations (OGS) expected to achieve of 99.5+% availability [2]. Despite the potential of OFL, reliable propagation of optical waves through the atmosphere remains a challenge, with strongly varying attenuation, absorption and turbulence impacting signal quality and risks of OFL outages. Site-diversity and related network management are key to meet 99.x% link availability, as required for VHTS applications [3].

* r.saathof@tudelft.nl; Telephone: +31 15 27 85518, https//www.tudelft.nl/lr/laser-satellite-communications

1.2 Potential of Tundra satellite orbits

The assumption in current research is that VHTS are, per definition, placed in GEO. Consequently, this architecture has also been studied to cover high-latitude regions such as Europe [4] [5] [6].This orbit, however, is ill-suited to service high-latitude regions as it does not allow for sufficient elevation angles when establishing a link through the atmosphere from 50+ deg latitudes, excluding the placement of OGS at large economic hubs in Europe and Canada. Previous system studies on OFL to GEO discussed the effect of anisoplanatism on the effectiveness of ground-to-satellite link pre-compensation and identified a concerning compounded effect of large point-ahead angle and low link elevation to GEO.

An alternative architecture with two geosynchronous satellites in Tundra orbits, tailored for a long dwell time over Europe or Northern America, could provide continuous coverage with increased elevation angles at these high latitudes. The high link elevation of 50+ deg over Canada or Northern Europe will enable the deployment of optical ground stations at high latitudes and could yield a considerable link budget improvement by reducing atmospheric attenuation and turbulence penalties. This significantly improves the optical link budget and increases the data throughput and availability for OFL. The inclusion of more high-latitude OGS could furthermore open the way for new applications such as large-volume point-to-point optical data transfer for governmental users and data centres.

1.3 Study overview, scope and paper outline

This paper is Part II in a two-part series on Tundra satellite orbits for very high-throughput optical feeder links. Part I provides a comparison between a GEO and two-satellite Tundra mission covering Europe, with an in-depth study of the uplink performance with AO pre-compensated time series of the received optical power at the space terminal and a simulation of coherent intradyne receiver performance. This includes analysing the mission geometry, coverage maps, Sun exclusion and eclipses and an evolution of key link metrics over the full geosynchronous orbital period.

Part II analyses the feasibility and competitiveness of Tundra orbits with respect to GEO considering coverage, radiation and *dv* performance in an application study over Canada. This includes an in-depth comparison of a two-satellite Tundra and GEO mission and addresses on top level the link degradation under atmospheric turbulence. Special attention is paid on anisoplanatism effects on pre-compensation where a model is derived that compares to earlier findings validated by double-star measurements. A top-level link budget comparison shows availability improvements gained by moving from a single GEO to a two satellite Tundra constellation.

2. METHODOLOGY

2.1 Optical feederlink budget

This paper will focus on the link budget effect of moving the VHTS from GEO to Tundra and the impact on the high-throughput optical feeder link performance. Consequently, the performance of the user link is left outside the analysis. To place the OFL performance in the context of a generalised interpretation of the Quality of Service (QOS) requirements and performance metrics, the following three VHTS implementations serve as background:

- Broadband/broadcast service: Providing internet or telecom connection to regions not covered by terrestrial infrastructure.
- Fibre in the sky entry point: Provide ground-space data transmission as entry and exit point for space based optical networks.
- High-volume point-to-point transmission: Optical transmission of very large data volumes of opportunity through a bent-pipe architecture, relevant for secure data transmission for governmental- and data centre users

When defining the architecture, a single GEO satellite is compared to two satellite constellations in Tundra orbits. The above idea is to aggregate on each satellite multiple laser communication terminals to achieve a total 1 Tb/s throughput. A segmentation of the ground-based apertures over two or more pointing assemblies ensures a stepwise satellite hand-over for a Tundra constellation. A network of OGS offers continuous cloud free line-of-sight spread over the coverage area of interest.

In order to derive the link budget calculations, we first provide the configuration in Sec 2.2. We consider atmosphere attenuation in Sec. 2.3. We will look in detail on the attenuation that is caused by atmospheric turbulence. The turbulence profiles are defined in Sec. 2.4. We collected some temporal statistics of the turbulence in Sec. 2.5. As optical feederlinks will likely use Adaptive optics, we go in detail on the pre-correction capabilities, i.e. considering the anisplanatic effects in Sec. 2.9.

2.2 Analysis configuration

In the configuration of the optical link under analysis, the signal wavelength is considered to be in the optical C-band around 1550 nm, following CCSDS and ESTOL standards, among others benefiting from a wide atmospheric transmission window [7], commercial hardware availability and laser safety considerations [8]. Next, owing to the analysis of high data rate links, receiver detection is performed assuming commercially available telecommunications transceivers allowing for 100 Gbit/s per optical wavelength channel, as discussed in more detail in PART I [9]. Atmospheric attenuation and turbulence are the central challenge for space-ground optical feeder links and we consider a more benign 70% confidence case and a challenging 95% confidence case for turbulence conditions in our analysis.

2.3 Atmospheric attenuation

Atmospheric channel attenuation by molecules and aerosols adds a static signal loss, notably significant at low elevation angles. Data from the AERONET database provides a confidence level for the aerosol attenuation in urban areas at zenith: -0.4 dB and -1.6 dB for 70% and 95% respectively [10]. With the molecular attenuation given by the U.S. Standard atmosphere composition transmission computed in Lowtran: -0.063. In our link budgets an overall attenuation penalty of -3dB at zenith, including thin clouds, is considered and extrapolated using Lambert's Law.

2.4 Atmospheric turbulence

Random and dynamic variations in the refractive index of the atmosphere due to temperature fluctuations in mixing air masses impact the propagation of light beams. The optical signals propagating through these turbulent layers experience phase shifts, intensity fluctuations, and beam wandering, degrading the quality and reliability of the communication link.

The turbulent condition of the atmosphere is represented here using the refractive index structure constant $C_n^2(h)$, indicating the variation of the refractive index due to small fluctuations in temperature along the propagation path. While the exact vertical profile largely depends on local conditions, the Hufnagel-Valley is generally accepted for sizing studies as a baseline profile for mid-latitudes. Here adapted for a profile h_0 meter above sea-level by Giggenbach [11]:

$$C_n^2(h) = 0.00594\left(\frac{v}{27}\right)^2 (10^{-5}h)^{10}e^{-h/1000} + 2.7\cdot 10^{-16}e^{-h/1500} + A\cdot e^{(h-h_0)/100}, \qquad (1)$$

where v and A are the rms wind-speed (m/s) and C_n^2 ($m^{-2/3}$) at ground-level, respectively.

The Hufnagel-Valley 57 turbulence profile, representing the Fried parameter $r_0 = 19cm$ and the isoplanatic angle $\theta_0 = 24\mu rad$ at a wavelength $\lambda = 1550nm$ characterizes the link performance in many system studies. Based on long-term turbulence measurements across the United States by Walters [12], accounting for a reduction of factor 2.16 in mean r_0 during daytime [13], this condition is found to represent a 70% confidence level (approximately).

Table 1, Atmospheric conditions summary/

Conditions at zenith	Atmospheric attenuation	Atmospheric turbulence
Benign - 70% confidence level	-0.46 dB	r_0 : $19cm$, θ_0 : $24\mu rad$
Challenging - 95% confidence level	-1.66 dB	r_0 : $7.7cm$, θ_0 : $12\mu rad$

With the design of an OGS network driven by cloud-free line-of-sight probability to achieve a consistent availability of 99.9+%, a more robust margin is required to prevent the need for additional site-diversity for turbulence mitigation. Coupled analysis of cloud probability and turbulence in Japan has shown that small-to-no turbulence link margins can reduce the availability of an OGS network with up to 10 percent points [14]. Considering the variability of atmospheric turbulence conditions, and the need for continuous operations given a cloud-free line-of-sight, stronger turbulence conditions are to be included in link budgets for system proposals. A 95% confidence level during daytime in winter from long-term measurements at the Calern observatory has been chosen, with $r_0 = 7.7cm$ and $\theta_0 = 12\mu rad$ at

λ = 1550*nm*. To be represented as a Hufnagel-Valley profile scaled with ground-level turbulence and rms wind velocity of A = 6.0*e*− 14 $m^{-2/3}$ and v = 33.3*m/s*., which will be referred to as HV* in this paper.

2.5 Temporal characteristics of the isoplanatic angle

The variability of the isoplanatic angle is of concern as it is one of the key performance drivers of the uplink in an optical space-ground feederlink system. A collection of data sources describing main features is depicted hereafter.

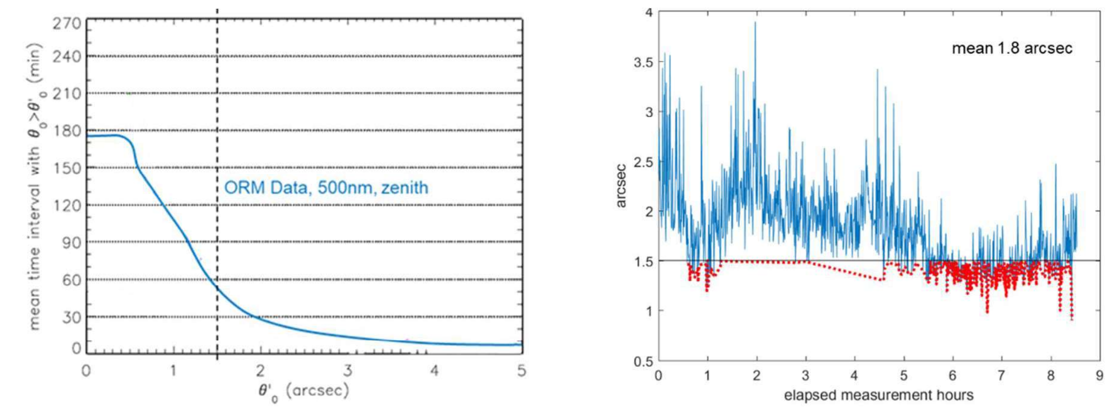

Figure 1: Temporal characteristics of the isoplanatic angle θ_0, minute-scale SCIDAR measurements.

The left part of Fig 1-1 is extracted from [15] and depicts the mean time_interval for the isoplanatic angle θ_0 (at 500nm, in zenith) remaining greater than a threshold θ_0' , based on aggregated measurements distributed over 1 year during. The right part shows an example of an hourly variation of θ_0 (500 nm, zenith), recorded at the Izana site at ESA OGS using the NSM of Miratlas. An arbitrary threshold was set to 1.5 arc sec.

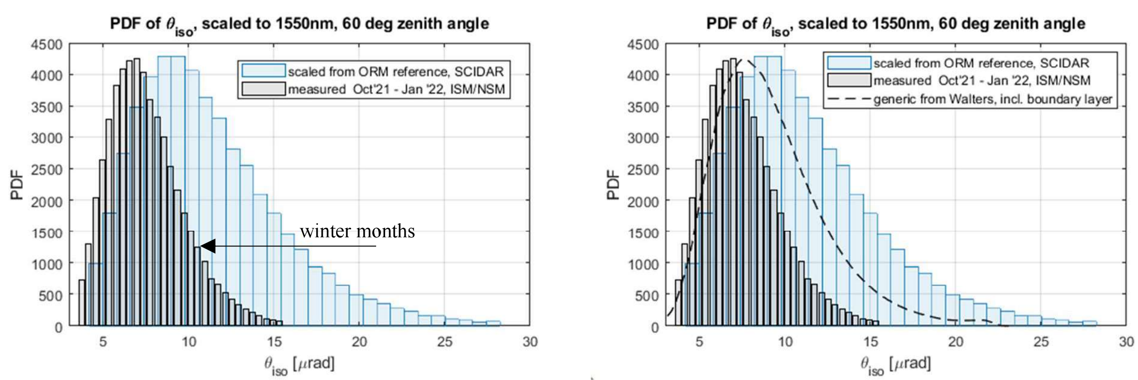

Figure 2: Seasonal impact on θ_0 variation.

The left part of Fig 1-2 depicts a reference histogram recorded over 1-year at ORM [15] in comparison to measurements collected over 3 winter months 2021/2022 using the NSM of Miratlas NSM at ESA OGS (Izana site). Both histograms were scaled to 1550nm, 60 deg zenith angle, microradian, in context of laser communications.The right part of Figure 1-2 includes a generic θ_0 distribution [12], based on measurements at 18 sites over 2 decades, including the presence of a boundary layer. Scaled to 1550nm, 60 deg zenith angle.We added the reference fromWalters [12] as a longer term gobal statistics input because Ramio et.al. [15] concluded for various reasons that a 1-year measurement campaign, though thoroughly mde, might not suffice for capturing seasonal statistics fully accurately. However, once put in context of a communications infrastructure, an OFL system should be able to cope also with the isoplanatic conditions captured by the measurements during winter 21/22. When comparing isoplanatic angle measurements from site characterization campaings at different altitudes [12], the lognormal distributed global statisitcs get close to each other. This suggests to consider in a first step tropopause impact as the main influencing atmospheric layer on isoplanatic angle variations, which in turn allows to neglect surface layer impact for first cut estimates of its pricnipal characteristics. We find also that lots of long term (seasonal) data samples capture as well short term (minute scale) variability. In that context it gets less important to compare daytime versus nighttime measurements.

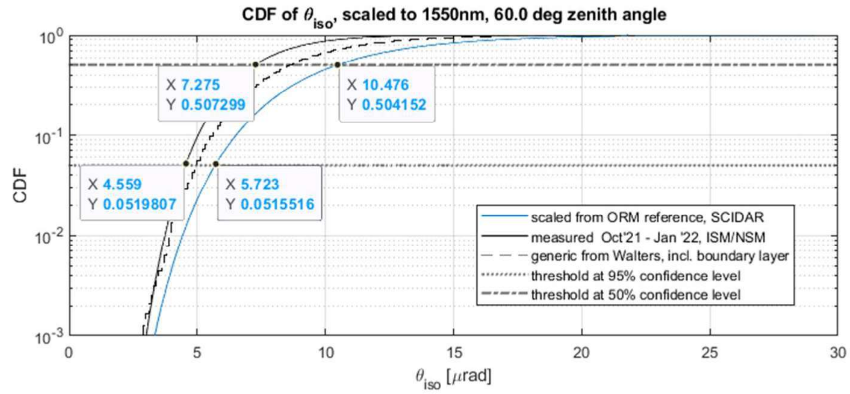

Figure 3: Cumultive distribution functions of θ_0 histograms depicted in Fig. 1-2: rather narrow variations at high confidence levels, independent from seasonal impact, but a pronounced seasonal impact on the median of θ_0

As a finding from above data collecitons, the selected isoplanatic angle from Calern is considered representative also for short-term diurnal fluctuations.

2.6 Adaptive optics

This link budget includes the commonly considered techniques of aperture averaging and adaptive optics pre-compensation to enhance the link reliability under turbulence conditions. In moderate and strong atmospheric conditions, high order adaptive optics compensation is much more effective [16]. This got demonstrated in a recent uplink measurement campaign to Alphasat [17]. An improvement of 10d B is reported for a high order AO correction when compared to tip-tilt-only correction, at a Fried parameter at 1064 nm, $r_{0,1064\text{nm}} < 5cm$ at $p < 10^{-1}$. However, also little perceivable improvement from high order AO on the uplink irradiance received in space is visible, even under weak boundary layer turbulence ($r_{0,1064\text{nm}} = 6-14cm$). The consistency of the statistical turbulence loss distributions under these conditions is remarkable and it could be attributed to high-altitude turbulence remaining uncorrected. This is an expected phenomenon for so-named 'classical AO pre-correction' and it is caused by the point ahead angle of the link to GEO leading to a decorrelation of uplink and downlink paths at high altitude, referred to as anisoplanatism. Strong high-altitude turbulence can this de-correlate the two wavefronts to such an extent that AO pre-correction would have an adverse effect. Full AO correction will degrade quicker under the influence of anisoplanatism [18].

2.7 Signal scintillation

Signal power fluctuations will occur, which causes fades at the receiver due to beam-wander and signal interference induced by propagation through atmospheric turbulence. To estimate these effects on a finite beam for both uplink and downlink paths, analytical and semi-empirical methods adapted from the general Rytov approximation have been implemented. Providing a scintillation margin for which, with probability p, it can be said that the signal power would not fade beyond that margin. We limit here the scope of discussion on uplinks which represent the primary design driver of optical space-ground feederlink systems.

The statistical distribution of log-amplitude uplink variance, σ_χ^2, for large beam diameters D including AO pre-compensation, we extended the method outlined for tip-tilt pre-compensation by Parenti/Sasiela in [19] which is also recommended in [20]. Their method had been verified by wave-optics simulations and it is reported to have been tested with horizontal and vertical links. An alternative method derived by Andrews [21] leads to same distributions and confirms the overall theoretical approach, providing a sound basis to start from.

The composite PDF from [19] is used as a baseline. It weighs the relative impact of Far Field distribution by p_{FF} and of near-filed distribution by p_{NF}, depending on the state of turbulence, It uses p_{FF} as log-normal distribution and p_{NF} based on a modified Nakagami distribution that can adapt to a Weibull distribution in case of tip-tilt pre-compensation.

$$p(S) = \frac{[\sigma_I^2]_{FF}^2 \cdot p_{FF}(S) + [\sigma_I^2]_{NF}^2 \cdot p_{NF}(S)}{[\sigma_I^2]_{FF}^2 + [\sigma_I^2]_{NF}^2} \tag{2}$$

The formula had to be extended for slant path geometries at a zenith angle ζ different from 0° or 90° as used in [19] While tup-tilt compensated uplink performance is discussed in this paper, an additional extension was implemented for the complementary analysis using higher order modes adaptive pre-compensation in PART I.

2.8 Signal strehl

To obtain the average effective loss of the link, we obtain signal Strehl. We assume a perfect Adaptive Optics system. In the analysis below, we first derive an expression to determine the residual phase variance, and compare it to a simple expression using the isoplanatic angle. Next, we remove piston from the phase variance, to make it more representative for a real system. Next, we look for confirmation in the literature, by comparing the contribution of tip-tilt errors with experiments on a binary star.

For an electromagnetic wave propagating from ground to space, both phase and amplitude scintillation variance are derived, starting at the Rytov method that expresses the electromagnetic field E as a function of parameter ψ

$$E = exp(\psi),\ \psi\ =\ \chi\ + i\varphi,\ \ \chi\ \equiv\ log(A) \tag{3}$$

With A is the field amplitude and φ is the field phase. The overall method is outlined in compact form, starting at equation 3.81 in [22].

The Strehl ratio is used conventionally as a performance criterion in adaptive optics systems. Phase and (log-) amplitude scintillation variance $\sigma_\varphi^2, \sigma_\chi^2$ are used in combination with the extended Marechal approximation (see section 4.3.3. in [22]), to estimate average Strehl losses for uplink modelling. Appropriate distribution functions have to be added for both variances.

$$S\ =\ exp\left(\sigma_\chi^2\ + \sigma_\varphi^2\right) =\ exp\left(\sigma_\chi^2\ \right) \cdot exp\left(\sigma_\varphi^2\right) \tag{4}$$

Sasiela derived the following set of equations to calculate both variance terms [20]

$$\begin{bmatrix}\sigma_\varphi^2\\ \sigma_\chi^2\end{bmatrix}\ =\ 2\pi\ \cdot 0.033 \cdot k^2 \cdot \int_0^L C_N^2(z) \int f(\kappa) d\kappa\ \begin{bmatrix}C_p\\ C_a\end{bmatrix} \prod_i F_i(\kappa, z)\, dz, \tag{5}$$

where the transverse turbulence spectrum *f(k)* for many cases is approximated by the Kolmogorov spectrum and in our numerical simulations gets replaced by the extended Von Karman spectrum [22]. The scalar $k = \frac{2\pi}{\lambda}$, and the functions Cp and Ca specify the beam convergence. For the analysis considered here, diffraction impacts are neglected, which allows to replace both coefficients with '1'. Eventually, the final term Fi represents the product of transverse spatial filters which are built in to represent certain aspects of adaptive optics pre-compensation.

We start by obtaining the benchmark, so we can compare Eq. 4 with known theory, i.e. without transversal filtering. This represents a perfect AO pre-compensation system, where piston errors are assumed to be relevant. So the residual phase distortion of a pre-compensated uplink beam, without filtering for piston and tip-tilt is:

$$\sigma_\varphi^2 = 2\pi \cdot\ k^2 \int_0^L C_N^2(z) \int_0^\infty f(\boldsymbol{\kappa}) \cdot 2 \cdot [1 - \cos(\boldsymbol{\kappa} \cdot \boldsymbol{d})]\, d\boldsymbol{\kappa}\, dz,\ z = h \cdot sec\zeta \tag{6}$$

This follows after solving the vector wave equation, using the phase variance of anisoplanatism as derived in [20]. Including the anisoplanatism penalties for feederlinks, requires to define the phase. This is represented by including the relation $d = z \cdot \theta_{PAA}$. The 2-dimensional integration along **κ**-space is commonly carried out in polar coordinates with aligning the radial component along one axis. We write down the following identity:

$$\int_0^{2\pi}\int_0^{\infty} 2\cdot[1-\cos(\kappa\cdot cos(\theta_{PAA})\cdot d)]\cdot\kappa\cdot d\kappa\, d\varphi \;=2\cdot 2\pi\cdot\int_0^{\infty} 2\cdot(1-J_0[\kappa\cdot z\cdot\theta_{PAA}])\cdot\kappa\cdot d\kappa \qquad (7)$$

This identity is used in Eq 4, to define the following baseline equation:

$$\sigma_\varphi^2 = 2\pi\cdot\; k^2\int_0^L C_N^2(z)\int_0^{\infty} 0.033\cdot f(\kappa)\cdot\kappa\cdot 2\cdot 2\pi\cdot(1-J_0[\kappa\cdot z\cdot\theta_{PAA}])\, d\kappa\, dz \qquad (8)$$

By assuming equation Kolmogorov spatial frequency spectrum, we cross-checked the equation with a numerical simulation by comparing σ_φ^2 to the same quantity once it gets derived without any transverse spatial filtering [20].

$$\sigma_\varphi^2 = \left(\frac{\theta}{\theta_0}\right)^{5/3}, \quad \theta_0 = 0.058\cdot\;\lambda^{6/5}\cdot cos^{8/5}(\xi)\cdot\left[\int_{h0}^{H} h^{5/3}\cdot C_N^2(h)dh\right]^{-3/5} \qquad (9)$$

2.9 Derivation of the phase error after AO pre-correction

So far, the analysis is done, without taking into account the effects of piston, tip and tilt. In practice, piston is not relevant, as it does not contribute to the Strehl ratio, but the tip-tilt does, as a normal laser guide star cannot compensate for tip-tilt aberrations. To proceed, we define the filter functions in Eq. 9. by taking the square of the absolute value of the Fourier transform of the spectral representation of the of Zernike modes derived by Noll. For Zernike polynomials expressed in polar coordinates by azimuthal frequency *m* and radial degree *n*, Sasiela presents a set of generic equations for an optical aperture diameter *D* – which in this case, represents the diameter of the transmitter. In this paper, we only present the filter functions for piston:

$$F_0(\kappa) = \left[\frac{2J_1(\kappa D/2)}{\kappa D/2}\right]^2 \qquad (10)$$

and the overall tilt components of the wavefront are defined by

$$\left.\begin{array}{r} F_x(\kappa)\\ F_y(\kappa)\\ F_{radial}(\kappa)\end{array}\right\} = \left[\frac{4J_2(\kappa D/2)}{\kappa D/2}\right]^2\cdot\left\{\begin{array}{c}\cos^2(\phi)\\ \sin^2(\phi)\\ 1\end{array}\right. \qquad (11)$$

The two-axis phase variance of anisoplanatism after piston removal is the quantity of interest. This is the phase variance at the satellite, when tip-tilt pre-compensation is not applied. Important in this context is to connect the effective Gaussian waist ω_0 to '*D*' via $D = \omega_0\cdot\sqrt{8}$. This also means, the telescope aperture is not clipping the uplink beam. The equation yields:

$$\sigma_{PR,\theta}^2 = 2.606\, k^2\int_0^L C_N^2(z)\int_0^{\infty} f(\kappa)\cdot(1-J_0[\kappa\theta z])\cdot\left[1-\left(\frac{2J_1[\kappa\, D/2]}{\kappa\, D/2}\right)^2\right] d\kappa\, dz \qquad (12)$$

The average Strehl penalty, after AO pre-correction; taking into account angular anisoplanatism (S_{IPA}), due to the point ahead angle, is obtained using the extended Marechal approximation of the phase aberrations after piston removal via $\sigma_{PR,\theta}^2$:

$$S_{IPA} = \exp(-\sigma_{PR,\theta}^2) \qquad (13)$$

So this result we use for obtaining the link loss of the AO pre-compensated uplink.

2.10 Comparison with experimental data

To compare the derived methodology with experiments by Alaluf [23], we derive the anisokinetic penalty. Anisokinetism is equivalent to anisoplanatism, with the difference, that for anisokinetism applies to tip-tilt aberrations only. In other words: the anisokinetic angle is the angle in which the phase variance of the residual tip tilt error is 1 rad^2. The aniso*kinetism* penalty is a fundamental limit for ideal higher order AO performance: once a laser guide star would allow for correcting all higher order modes, as an LGS cannot sense tip-tilt, the *phase* variance caused by tip-tilt aberrations only $\sigma^2_{T,\theta}$ is:

$$\sigma^2_{T,\theta} = 2.606\, k^2 \int_0^L C_N^2(z) \int_0^\infty f(\kappa) \cdot \left(\frac{4J_2[\kappa\, D/2]}{\kappa\, D/2}\right)^2 (1 - J_0[\kappa \cdot z \cdot \theta_{PAA}])\, d\kappa dz \tag{14}$$

This variance is relevant for perfect AO correction in combination with a laser guide star. The Strehl after perfect AO correction, using a laser guide star, also disregarding the focal anisoplanatism is:

$$S_{IKA} = \exp\left(-\sigma^2_{T,\theta}\right) \tag{15}$$

With S_{IKA} the Strehl related to the isokinetic angle. A tilt *angle* variance $\sigma^2_{T,\alpha}$ can be derived using the relation between the wavefront variance of tip-tilt aberrations with an angle $\sigma^2_\varphi = (\phi D/4)^2$ and assuming ϕ is representing the average standard deviation of tip-tilt errors:

$$\sigma^2_{T,\alpha} = \sigma^2_{T,\theta} \cdot \left(\frac{4}{k \cdot D}\right)^2 \tag{16}$$

Given that the tip and tilt Zernike representation are Gaussian weighted for a Kolmogorov spectrum[18] and that the derivation of the extended Maréchal approximation is based on the assumption of a Gaussian distributed phase error.[31] this seems to be a reasonable approximation. Inserting into equation 14 yields for the anisoplanatic tilt angle variance σ^2_{TA}

$$\sigma^2_{T,\alpha} = \frac{41.696}{D^2} \int_0^L C_N^2(z) \int_0^\infty f(\kappa) \cdot \left(\frac{4J_2[\kappa\, D/2]}{\kappa\, D/2}\right)^2 (1 - J_0[\kappa \cdot z \cdot \theta_{PAA}])\, d\kappa dz \tag{17}$$

As confirmed by comparison to wave-optics simulations, this equation is valid for a small phase variance close up to 0.3. This approach allows for a direct comparison to the method reported by Alaluf/Perdigues that got validated by Double-Star measurements, shown in Fig. 4, which shows the approximations are close.

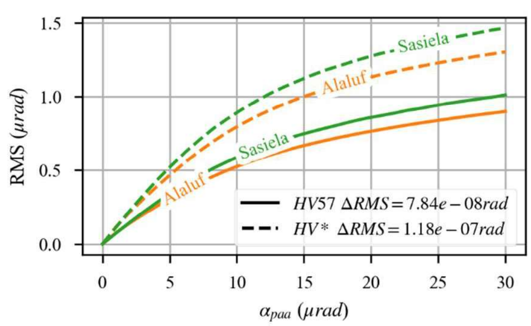

Figure 4: rms phase tilt error for Alaluf and Sasiela method.

2.11 Canada Case study

A case study was conducted to examine the application of Tundra orbits for enhancing coverage across Canada and integrating with a domestic optical ground station network This analysis focuses on the performance of optical feeder links to a Very High-Throughput Satellite system, utilising a network of nine OGS sites confined to Canadian territory as outlined by Gagnon et al. [24], achieving a cloud-free line-of-sight availability of 92.9%. While this is insufficient for general optical feeder links QOS, this network is assumed for a baseline comparative analysis of Tundra orbits implementation. Yet, it is noted that expanding this network, as demonstrated by similar high latitude OGS networks in Europe - including cities like Oslo, Berlin, and Birmingham - could potentially increase availability to 99.5% for 11 OGS [6].

Connecting these Canadian OGS sites to VHTS in GEO poses significant challenges due to the low elevation angles encountered at high-latitudes, as depicted in Figure 3a. Gagnon et al. recognise the challenge of this GEO-ground link at high-latitudes and suggest alternatives such as OGS abroad and GEO-HAP (High Altitude Platform) links. Optical feeder links located in Canada could benefit from the effective high-latitude coverage of Tundra orbits, not necessitating the deployment of OGS abroad or the deployment of expansive LEO constellations with global coverage. In the following section the selection of a suitable Tundra orbit for a two-satellite constellation for coverage of this OGS network will be performed. Additionally considering the coverage of satellite-dependent communities in Canada [25] as a possible use-case with Tundra VHTS providing backhaul or broadband connectivity. The scope of this use case includes a preliminary coverage analysis for these user links. Comprehensive performance evaluations of these links are left for future analysis.

2.12 Tundra orbit properties

Geostationary orbits are characterised by their fixed position at the equator, as seen from an observer on Earth, due to a zero inclination and a period equal to Earth's rotation. Tundra orbits have a similar geosynchronous period. However, an observer on Earth will see the satellite rise to the zenith and fall over the horizon in the course of a day due to a slight eccentricity and a high inclination. The benefit of a Tundra orbit stems from its long dwell time over high-latitude regions, given an argument of perigee of 270 degrees and the non-zero eccentricity. This lower velocity at apogee, coupled with the rotation of the Earth, gives a Tundra ground track the characteristic loop at northern latitudes.

The orbits are to be optimised for the OGS network under evaluation. For such a geosynchronous orbit, the semi-major axis is naturally fixed at 42,164.7 km, and an argument of perigee of 270 degrees is chosen to maximise satellite dwell time over Northern latitudes. The longitude of the ascending node is chosen at 270 deg for an apogee centred in Canada. This arrangement leaves eccentricity and inclination as the primary variables to be determined. In selecting an orbit for these constellations, our criteria are as follows:

1. Maximisation of optical link performance: The orbit must enhance the performance of optical links, increase data rate and availability across the coverage region.
2. Feasibility and competitiveness relative to GEO: Maintain orbit cost and environment as good as GEO or with minimisation of the required mitigations.

2.13 Orbit ΔV characteristics

Orbit insertion, EOL and station keeping cost provides a metric to constrain the design space. In the absence of long-term numerical propagation and details on launch date a general argument on orbit ΔV costs is made.

For orbit control costs, a ground-track-only maintenance strategy is chosen. Maintaining stable phasing and argument of perigee, while allowing eccentricity and inclination to vary. Fantino et al. performed numerical propagation showing a maximum two-year variation of 0.07 in eccentricity and 1.2 deg in inclination [26]. From the Tundra orbit coverage performance in Figure 5a this is shown to have minimal impact on coverage.

An inclination of 63.4 degrees minimises the required yearly control of perigee positions due to the J2 perturbation. Additionally, third-body effects might allow for the selection of frozen orbits based on individual orbit RAAN-inclination-eccentricity combinations. While such orbits offer reduced ΔV costs for maintenance, these would also potentially maintain prolonged stability in their graveyard orbits, failing to de-orbit within the prescribed 200-year period. Consequently, due to time constraints and the required coupled analysis of long-term operation and EOL stability, this strategy has not been pursued. Subsequently the design space has been limited to the J-2 frozen orbit 63.4 deg inclination.

Orbit insertion and EOL exhibit slight variations, favouring lower eccentricities or higher eccentricities depending on the employed EOL strategy. Since orbits are inserted into their respective planes via separate launches, inclination does not significantly impact orbit insertion costs. Higher eccentricity does however benefit the efficiency of the impulsive manoeuvres. If one would consider the Near-Tundra Orbit strategy, this benefit for eccentricity stands. However, if there is a strict de-orbit and GEO clearing requirement circularising at apogee would on the other hand benefit eccentricity. Consequently, pending such detail this is considered as a neutral argument in orbit selection.

2.14 Orbit radiation and charging environment

The orbital radiation and charging environment of Tundra orbits provides limits to the sustainable operations in these orbits without requiring significant modifications from GEO-rated hardware. The spacecraft radiation environment has been analysed for geosynchronous orbits providing sufficient dwell time to Northern latitudes. This analysis has been performed using the SPENVIS tool developed by ESA [27], following a methodology similar to that presented by Trichtchenko [28] in analysing highly eccentric orbits. Implementing trapped electron and proton particles, solar protons, heavy ions and Galactic Cosmic Rays. Appendix A includes a detailed description of the results. The deep charging effects in Tundra orbits are relevant for orbit selection, highlighting the risk of deep electric charging at high eccentricities beyond 0.3. Conversely, orbits with eccentricities below 0.2 demonstrate substantial improvements in these respects when compared to traditional GEO operations. Total Ionization Dose analysis shows a mean reduction of 40 % across Tundra orbits with respect to GEO. Additionally, changes in geomagnetic shielding from GEO orbits have been shown to have negligible impact on predicted worst case Single Event Upset rates. Based on these insights, the inclination-eccentricity design space for Tundra orbits can be sustainably maintained up to an eccentricity of 0.3 (depending on inclination angle, see Appendix A), offering a viable range for sustainable long term satellite operations.

2.15 Coverage

For each orbit the link geometry to the optical ground station network in Canada has been generated, storing link length and link elevation angle offered by the two-satellite constellation. From this the limiting link for each location, representing longest link length (at apogee) and lowest link elevation (at handover) is considered as a coverage performance indicator. The minimum and mean limiting links over all OGS are presented in Figure 5a.

From this analysis, the following predictable result is visible: higher eccentricity orbits tend to increase both the mean and limiting elevation angles. Furthermore, we see that the optimal inclination for maximising coverage lies between 55 and 75 deg. Supporting the choice for a frozen inclination orbit at 63.4 deg. The evaluation of orbit implementation has restricted the design space to an inclination of 63.4 degrees, while favouring an eccentricity a lower eccentricity to minimise radiation and charging effects. With the varying link geometry over time, one could consider two limiting optical link cases for each ground station:

- **Satellite hand-over (ho)** - point of minimum elevation
- **Satellite at apogee (ap)** - point of maximum link range

Reviewing the effects of slant path on atmospheric effects and link length on signal spreading, there is a necessary balance between maximising link elevation and minimising range to effectively minimise both atmospheric and free-space losses for each of these limiting conditions. To consider these cases in Tundra orbit selection, the coverage performance is defined by the limiting path-losses over the region/points of interest, defined as:

$$L_{path} = L_{FSL,ap}\, L_{atm,ho}\, L_{turb.mean,ho}\, L_{turb.scint<0.01,ho} \tag{18}$$

The bounds for 70% conditions and 95% turbulence levels, assuming an atmospheric attenuation of 0.46 dB, have been computed for varying eccentricity. The results of this analysis are depicted in Figure 5b, which illustrates the limiting link loss for the mean and worst OGS in the network. From this an orbit is chosen to minimise link losses to the OGS network at 95% conditions, giving an eccentricity of 0.3 at the inclination of 63.4 degrees.

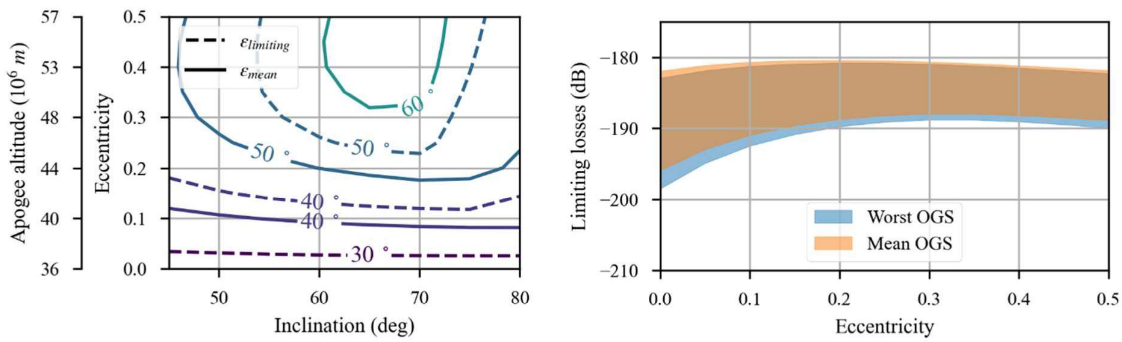

(a) Evolution of limiting link geometry over Tundra orbit eccentricity and inclination.

(b) Evolution of limiting propagation losses over 63.4 deg Tundra orbit eccentricity.

Figure 5: Link conditions over optical ground station network.

3. RESULTS AND DISCUSSION

3.1 Satellite orbits and coverage

The following section details the orbit characteristics of the selected Tundra orbits in comparison to a Geostationary satellite situated at 105 deg West. The two Tundra constellations selected provide excellent coverage and elevation angles over the optical ground stations locations and the satellite-dependent communities under consideration. In Figure 6, the minimum link elevation across the coverage region is presented, complemented by a skyplot in Figure 7 for the OGS at Vancouver, Esquimalt located on the Canadian west coast. The limiting link (lowest elevation angle to satellite) across the OGS network achieves a mean of 70.2 deg, compared to 29.5 deg for a GEO satellite. The worst link geometry is experienced by the most Eastern located ground station with a limiting link of 53.6 deg.

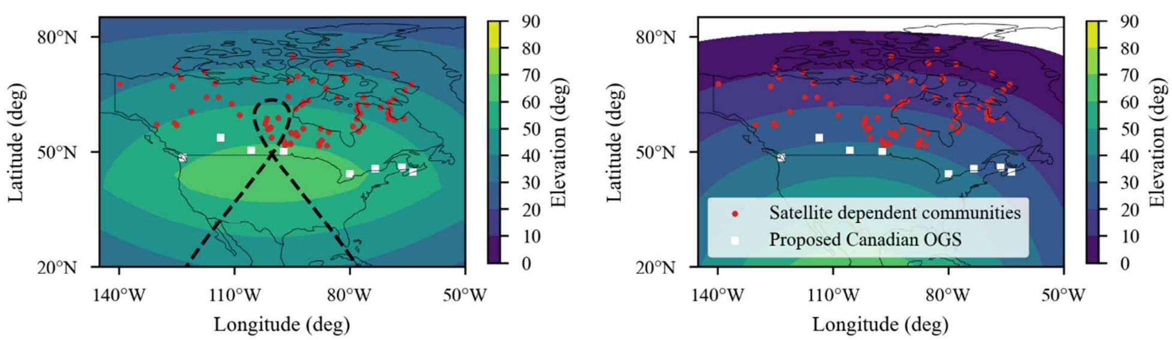

(a) GEO (105∘W) link elevation.

(b) Tundra (e:0.3, i:63.4) minimum link elevation.

Figure 6: Link geometry over region of interest.

While the Tundra orbit has been fitted to the OGS network, coverage of Satellite dependent communities across Canada benefit from a mean limiting-elevation angle of 71.1 deg, with the worst community having a limiting link elevation of 34.6 deg. This compares very favourably to GEO with a mean and minimum limiting link elevation angle of 18.6 and 3.9 deg respectively. The general characteristics are summarised in Table 2.

Table 2: Orbit characteristics summary.

Orbit characteristic (unit)	GEO 105 deg W	Tundra
Semi-major Axis (km)	42164.7	42164.7
Eccentricity	0	0.3
Inclination (deg)	0	63.4
Argument of Perigee (deg)	-	270
LAN (deg)	-	270/90
Mean Anomaly (deg)	-	0/180
ΔV control	44	41
ΔV insertion	1491	1171
ΔV end-of-life	11	13/436
TID 3mm Al (krad/year)	5.1	2.7
SEU 5min worst case 4mm Al (/bit/s)	0.0025	0.0025
Penetrating flux 10h mean 3.7mm Al (/cm^2/s)	1.04e6	1.28e6

Pointing simulations from Esquimalt indicate acceptable azimuth and elevation rate throughout the apogee pass. Notably, there are no significant accelerations due to changes in relative direction at the apogee. In Figure 7 the time relative to apogee is included, to be used to see the separation of the satellites in the constellations. A critical concern for optical communications is the Sun angle, where small angles increase background noise and could potentially damage sensitive equipment. The Sun path during the June equinox - highest pass at the northern latitude - has been included in the skyplot. Close approaches between the satellite and Sun path could be mitigated through strategic phasing, such as positioning the apogee at noon or planning handovers in the morning or afternoon. This does, however, require control of the mean RAAN motion of the constellation. Phasing the daytime orbit for an apogee at 12h is also interesting from a turbulence mitigation perspective to account for diurnal variations. A final differentiation factor between GEO and Tundra is the point ahead angle related to the tangential orbital velocity. The varying velocity in Tundra orbits causes this value to fluctuate from 18.2-15.1 µrad for two satellite a from handover to apogee, reaching its minimum at apogee.

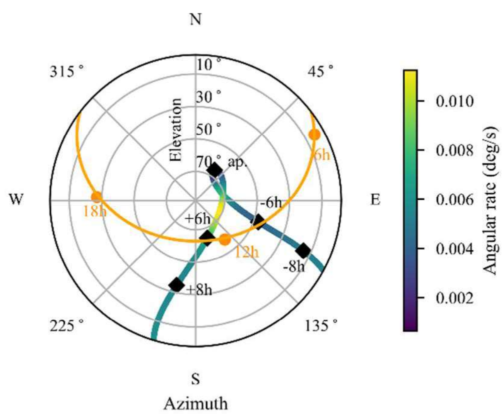

Figure 7: Skyplot Vancouver to Tundra.

Based on our analysis of the orbit characteristics, the selected Tundra orbits provide significant improvements in coverage, albeit with the requirement of deploying two satellites. Environmentally, these orbits are viable, maintaining acceptable radiation levels with minimal mitigation required for 0.3 eccentricity orbits to protect against deep charging effects encountered during daily transits through the outer Van Allen belt. From a geometrical standpoint, the pointing requirements for Tundra orbits pose no significant challenges and sun-exclusion can be performed comparatively simply and effectively. Accommodations will have to be made for satellite handovers by the distribution of Tx and Rx apertures over separate pointing systems to minimise loss of instantaneous throughput.

3.2 Dynamic turbulence penalties

The current analysis focuses on the uplink where next to residual jitter-induced uplink pointing errors, dynamic turbulence penalties need to be accounted for that stem from residual wave front pre-correction errors. This section creates a connection to the complementary analysis in PART I by calculating corresponding turbulence key parameters over site locations in Canada. We consider the range up to 60 deg North a current potential limit, when allowing initial cloud-free line of sight analysis over Europe [6] to be assumed and still valid for this first cut analysis, yet to be done entirely for Canada.

For consistency to PART I we analyse the Fried parameter and the isoplanatic angle in a latitude range over Canada for the median elevation angle. A comparison to PART I shows comparable values for both, r_0 and θ_0 over the entire longitude/latitude range in Canada that lead to normalized dynamic turbulence penalties similar to those found and used for full adaptive optics pre-compensation link budgets analysed in PART I and apply as well to the link topology considered in this PART II study.

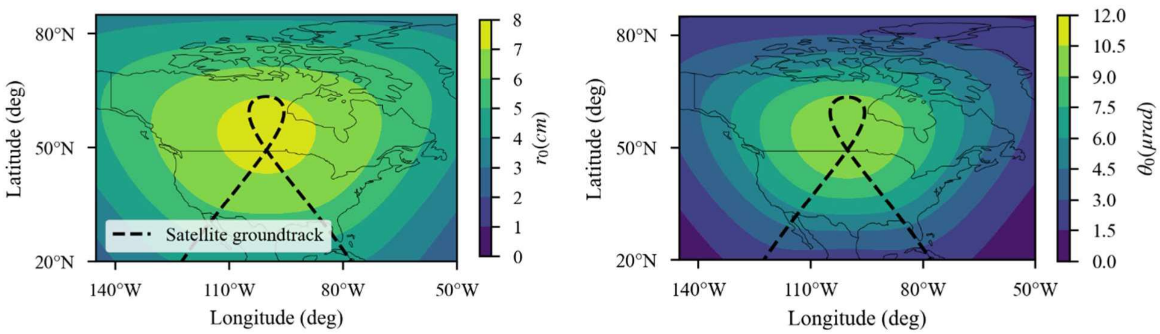

Figure 8: Key parameters for dynamic turbulence analysis over Canada at mean elevation angle – left: r_0, right: θ_0.

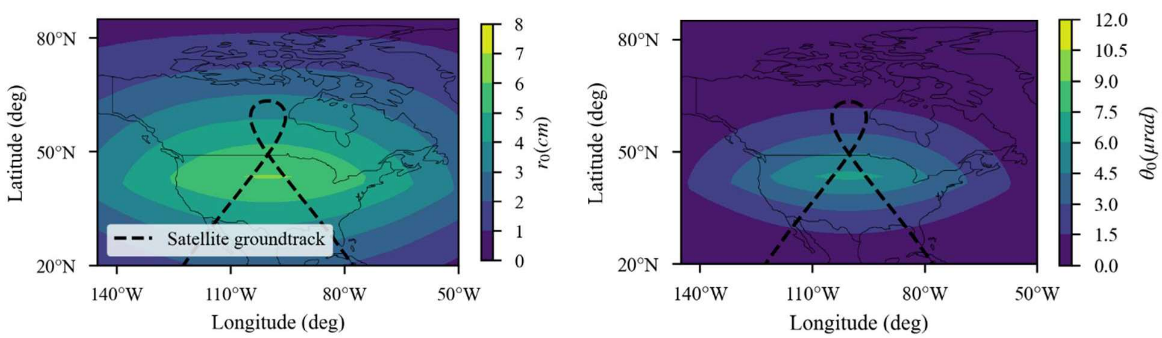

Figure 9: Key parameters for dynamic turbulence analysis over Canada, minimum handover-elevation– left: r_0, right: θ_0.

The following section elaborates on the accumulated mean uplink irradiance penalty that mainly consists of atmospheric transmission following Lambert's law and the average of corresponding dynamic turbulence penalties. In all cases, residual pointing jitter at the transmitter is assumed the same and thus not further discussed.

3.3 Tip/tilt pre-compensated uplink turbulence penalties

This section will discuss the results of the analytical modelling approach of signal scintillation and beam coupling losses, explicitly including anisoplanatic errors, and focus on the resulting median penalty derived from overall combined scintillation statistics combined from amplitude and phase distortions. The model we use compares to one derived from double-star measurements and is considered mature. In addition to a mean loss the statistical margin required to maintain scintillation fades are compared for uplink geometries to GEO and Tundra.

Following the analytical model of wavefront phase variance, the Strehl ratio was computed using the Extended Maréchal approximation. Giving coupling losses for a range of conditions representative for GEO and Tundra operations in Figure 10 with D = 20cm. Interpreting this figure, the α_{paa} = 0 case considers mean coupling error losses for tip-tilt pre-compensation without anisoplanatic effects and, following the trend along the x-axis showing the effect of anisoplanatic losses due to the point-ahead angle. Note how for high link elevation angles of 50+ deg the mean anisoplanatic induced losses are limited to 0.5-1 dB. At low elevation angles, the compounding effect of increased atmospheric propagation path with mean losses can be observed with 1-2 dB induced losses by anisoplanatism in even benign atmospheric turbulence conditions.

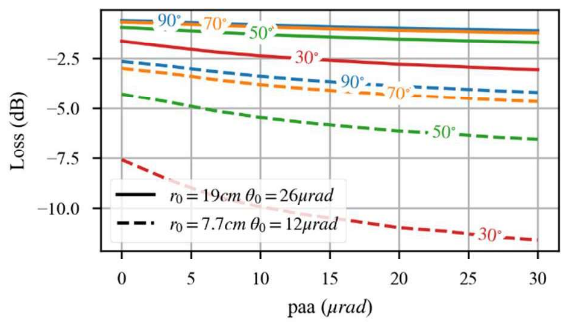

Figure 10: Mean turbulence losses, including anisoplanatism for varying elevation angle and αpaa=18.5µrad, D = 20cm.

Following the same uplink configuration as for the mean signal coupling losses, results pertaining to signal scintillation are discussed. The cumulative distribution function (CDF) of the fading probability for varying link margins is presented in Figure 11. Similarly to the mean losses, the expected increase in turbulence effects for low elevation links can be observed. Where for generally accepted fade probability of 0.01 under HV57 conditions, a GEO link at 30 deg would require a 7 dB scintillation fade margin. On the other hand, a Tundra link at 50 deg would require a 4 dB margin. A considerable reduction which grows even more so under stronger turbulence conditions.

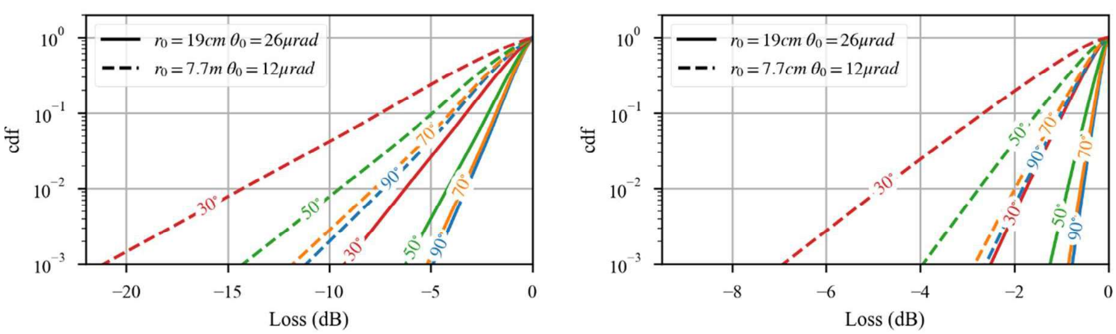

Figure 11: CDF of signal fades, α_{paa} = 18.5µrad D = 20cm, left turbulence fades right anisokinetic fade.

Due to the difference in the measured wavefront of the downlink to that of the pre-corrected uplink, tip-tilt jitter of the in-perfect tip-tilt AO correction will induce an additional anisoplanatism error. Implemented as a separate Rayleigh distributed CDF of the anisokinetic component Figure 12. Notable here is the stronger dependence on elevation angle than for ordinary scintillation. High elevation angle links show fewer losses even for stronger turbulence conditions than a 30 deg elevation link under HV57 conditions. Introducing an additional signal fade margin of -1.8 dB at 30 deg -0.5 dB at 50 deg for p<0.01 and HV57.This impact of anisoplanatism on the mean losses and scintillation margin highlights the importance of considering these additional losses in system designs. This is particularly critical for low elevation uplink of GEO, which ought to include a mean 1 to 2 dB additional link margin as well as a 1.8 to 3.2 dB scintillation margin. Reinforcing the value of high link elevation angles due to the compounding effect of turbulence losses and reduced effectiveness of AO on the effective signal power. Notably, a loss which cannot be mitigated and is expected to increase with higher order AO compensation.

3.4 Link budget results

The atmospheric penalties for an uplink from the Vancouver, Esquimalt ground station at 48.44 deg N 123.34 deg W is presented for the ordinary GEO and Tundra under benign 70% and challenging 95% confidence level conditions in Table 2. With uplink geometry of 31.6 deg elevation for GEO and 55.2 to 67.7 deg elevation to Tundra.

Table 3: Mean and 1% uplink turbulence penalties Vancouver OGS, Tundra results are given for *Handover*/A*poapsis*.

Parameter	GEO	Tundra	GEO	Tundra
	Benign 70%		Challenging 95%	
Mean turbulence loss (dB)	-1.6	-0.8/-0.7	-7.2	-3.6/-3.1
1 % scintillation loss (dB)	-5.1	-3.2/-3.0	-12.1	-7.4/-6.8
Mean anisoplanatism loss (dB)	-1.0	-0.5/-0.3	-3.0	-1.5/-1.3
1 % anisoplanatism loss (dB)	-1.6	-0.7/-0.5	-4.6	-2.4/-2.0
Static atmospheric attenuation (dB)	-0.86	-0.53/-0.49	-4.01	-2.47/-2.3
Total required margin	-10.16	-5.73/-4.99	-30.91	-17.37/-15.5

Under benign conditions, the Tundra constellation show significant improvements due to decreased atmospheric attenuation and turbulence losses totalling a reduction of 4.43 dB in atmospheric penalties with respect to GEO for 70% confidence level conditions. For high availability services, assessing the required link-margin for operation during 95% confidence atmospheric conditions reveals that GEO links will degrade dramatically. Requiring substantial uplink margins to compensate for 30.91 dB of penalties. The Tundra constellation, benefiting from high link elevation, require a considerably smaller margin of 17.37 dB.

Considering anisoplanatism penalties in the current configuration, a two satellite Tundra constellation would give a factor 2.77x increase in received power, enabling an equal increase in data rate under 70% confidence level. Operating under 95% turbulence conditions, required for continuous feederlink operations, will necessitate the closing of the link budget in Table 4.

Alternatively, additional site diversity can be considered to maintain continuous, introducing coupled low-turbulence and cloud-free line-of-sight statistics. To illustrate this effect the cloud-free line-of-sight availability of the Canadian OGS network [24] has been revisited. Adjusting the individual OGS probabilities to reflect a loss of 30% availability with a link margin for benign conditions and 5% with a margin for challenging atmospheric environment. The initial 92.16% availability of this 8 OGS network would then decrease to 87.14% or 91.92% without and with strong turbulence margin respectively.

The large projected impact of anisoplanatism losses for this 20 cm aperture uplink tip-tilt corrected configuration is notable. Which for the high elevation Tundra concepts corresponds to a 1.2 dB to 3.9 dB penalty, while for GEO it amounts to 2.6 to 7.6 dB, for HV57 and HV* respectively.

The link budget presented here for a ground station located in Vancouver, Esquimalt, Victoria Canada illustrates the comparative performance of the proposed Tundra constellation with respect to GEO. Significant improvements of the data rate under benign conditions justify the additional investment in launches and satellites from a $/bit perspective. Furthermore, requiring considerable smaller link margins to ensure operations in stronger turbulence scenario. Allowing for not only a reduction in size of the required OGS but also that of the OGS network to provide continuous availability.

Table 4: Link budget from the Esquimalt, Vancouver CA ground station to orbit under challenging atmospheric conditions, Tundra results given for Handover/Apoapsis respectively.

	Uplink		Downlink	
Parameter (Unit)	GEO	Tundra	GEO	Tundra
Link length (km)	38467	44213/48863	38467	44213/48863
Elevation angle (deg)	31.6	55.2/67.7	31.6	55.2/67.7
Point ahead angle (μrad)	18.5	18.2/15.1	0	0
Tx beamwaist (cm)		7.1		8.8
Tx gain (dB)		112.2		114.1
Rx diameter (cm)		25		25
Rx gain (dB)		114.1		120.1
Optical output power (dBm)		47		30
Transmitter loss (dB)		-4		-4
Pointing loss (dB)		-0.4		-0.63
Free-space loss (dB)	-289.9	-290.7/-291.2	-289.9	-290.7/-291.2
Atmospheric attenuation (dB)	-4.01	-2.47/-2.3	-4.01	-2.47/-2.3
Mean turbulence loss (dB)	-7.2	-3.6/-3.1	-10.4	-5.2/-4.6
Mean anisoplanatism loss (dB)	-3.0	-1.5/-1.3	0	0
Scintillation loss p<0.01 (dB)	-12.1	-7.4/-6.8	-10.8	-5.9/-5.3
Scintillation aniso. Loss p<0.01 (dB)	-4.6	-2.4/-2.0	0	0
Mean Rx power	-35.2	-29.4/-29.0	-44.7	-38.8/-38.5
99% Rx power (dBm)	-51.9	-39.2/-38.8	-55.5	-44.7/-43.8

4. CONCLUSION AND RECOMMENDATIONS

In this study, we have conducted a comprehensive analysis comparing the performance of Tundra satellite constellations with a traditional Geostationary orbit configuration for additional coverage of high latitude regions. With a general examination of orbital characteristics and detailed analysis of anisoplanatism and overall link budget performance.

Our investigation of anisoplanatism effects on mean and scintillation losses for tip-tilt corrected uplink budgets, revealed substantial link budget impacts. For the low elevation GEO configuration, losses for an OGS situated in Vancouver ranged from -2.6 to –7.6 dB. In contrast, links to Tundra with elevation angles beyond 50 deg would experience considerably lower losses, although still significant from -1.2 to -3.9 dB. These findings highlight the compounded atmospheric losses at low elevation angles and underscore the necessity of accounting for these factors in future satellite system studies for optical feeder links. Feasibility concerns of Tundra orbits have been addressed showing that for low-to-moderate eccentricity Tundra orbits exhibit lower accumulated radiation dosages, and comparable charging environments to GEO. Orbit insertion, end-of-life and station keeping cost have furthermore been shown to be as-good-as or better than GEO.

A case study focusing on very high throughput satellites using a domestic optical ground station network in Canada was conducted. A two-satellite Tundra orbit configuration have been optimised to maximise optical feeder link performance, selecting for a two-satellite system an eccentricity of 0.3 and inclination of 63.4 deg.

Our link budget analysis indicated that Tundra orbits significantly enhance data rates even under benign HV57 conditions, when compared to GEO offering increases of 2.44x and 2.14x for uplink and downlink received power respectively. Furthermore, while GEO operations in 95% probability turbulence conditions would require a significant additional link margin of 30.9 dB, leading to an unrealistic expansion of the ground segment of tip-tilt pre-corrected uplinks. Tundra constellations could maintain operations at same confidence level with an atmospheric penalty margin of 17.4 dB on the uplink. This suggests that a two-satellite Tundra constellation could remain operational under more challenging atmospheric conditions, whereas GEO would need to make use of diversity techniques necessitating the expansion of the OGS network or reducing network availability with up to 6 percent.

Overall, this study highlights the significant advantages of Tundra satellite constellations over a traditional GEO architecture for high-latitude services. Highlighting the impact of link elevation angle on optical link performance and how system design should adapt.

APPENDIX A. SPACE ENVIRONMENT

Each orbit under consideration has been generated in SPENVIS for a trajectory of 1 year, over which the radiation sources and effects are computed. The effects of Earth shadowing and geomagnetic attenuation of the particles are adjusted accordingly by SPENVIS, with the Earth magnetic field lines defined by IGRF-13 for 2020. A mixture of solar and magnetic conditions represent mean or extreme conditions for each radiation source were relevant.

A.1 TRAPPED PARTICLES

The fluxes and spectra of the inner and outer Van Allen Belts are considered using the AE9 and AP9 (v1.50) dataset [29]. An empirical model well suited for inclined and eccentric orbits due to the inclusion of measurements by two HEO missions [28]. The analysis of each orbit consists of the mean of seven orbits spaced at 60 deg RAAN to average out longitudinal variations in the Van Allen belts. Moreover, providing generalised results applicable to an entire constellation, irrespective of launch epoch or orbit RAAN. The mean proton and electron density are evaluated to provide long-term predictions of the total ionisation dose. The movement of satellites in three geosynchronous orbits has been illustrated in Figure 12, showing the pass through the outer radiation belt. An eccentric orbit is notably exposed to higher peak fluxes however, for a shorter duration. Note that AP8 and AE8 have been displayed in Figure 12, due to functionality limitations in generating a coordinate frame in SPENVIS.

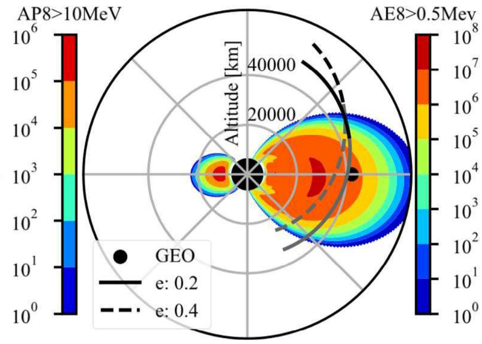

Figure 12 Trapped particles flux AP8 (left) and AE8 (right).

A.2 SOLAR PROTONS AND HEAVY IONS

Charged particles ejected by the Sun provide mean and peak fluxes to a satellite beyond the Van Allen Belts shielding. The mean ionisation impact of solar protons and solar heavy ions (H to U) has been modelled with ESP [30] and PSYCHIC [31], respectively. Evaluated during solar maximum with a quiet magnetosphere and a confidence level of 95% that this cumulative fluence of solar events is not exceeded. The peak solar particle flux, for a 5min worst-case SEU analysis follows from CREME-96, a dataset representing the worst week and worst 5 min averaged peak flux during the 1989 October solar flare, considered a 99% confidence-level worst-case event.

A.3 GALACTIC COSMIC RAYS

Galactic Cosmic Rays conditions are likewise based on CREME-96 [32] and corresponds to measurements of the last maximum of GCR observed in 1986-87. Corresponding to solar minimum conditions with reduced solar magnetic shielding, thereby increasing the intensity of Galactic Cosmic Rays observed in the heliosphere.

A.4 TOTAL IONISATION DOSE

The total ionisation dose integrated over a year could be determined using the SHIELDOSE-2 model [33] for a Silicone material shielded by a finite Aluminium slab. The ionisation effect of trapped particles, solar protons and Bremsstrahlung is considered. An aluminium shielding of 3 mm thickness was taken, equivalent to the required shielding in GEO, to achieve an acceptable 5 krad yearly dose. The resulting radiation dosage over the design space of Tundra orbits is then explored in Figure 13. The trapped proton effects of the inner Van Allen Belt have been omitted from this overview as these have been found not to affect high-altitude orbits.

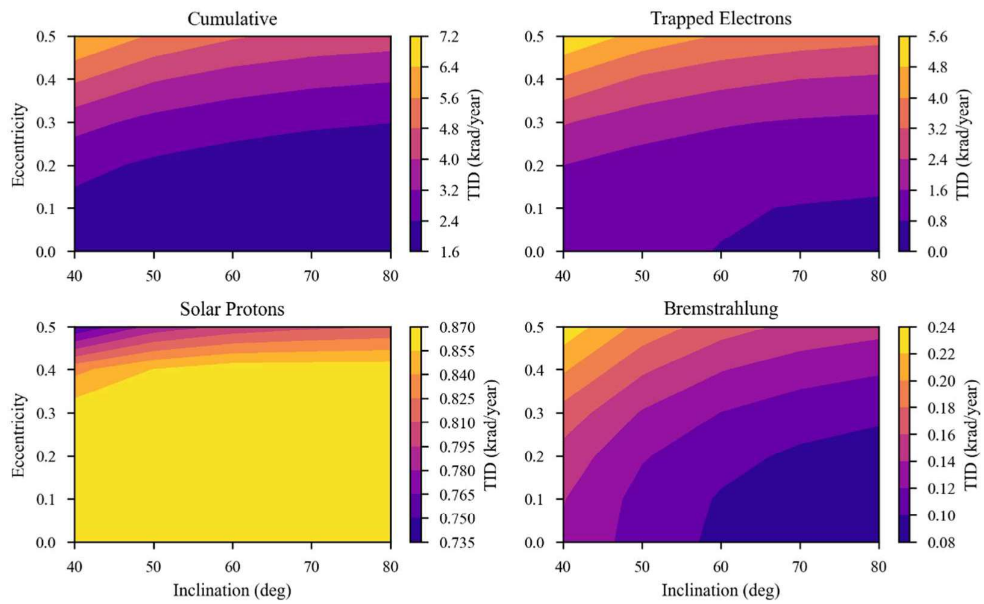

Figure 13 Yearly Total Ionisation Dose for Geosynchronous orbits.

The pass of eccentric and inclined orbits through the outer Van Allen Belt illustrated previously in Figure 12 results in a change in cumulative dose effect due to an increased intensity of electrons deeper in the belt. Large inclination orients the perigee more to the south pole and avoids more significant portions of the outer belt to reduce the integrated dose. Larger eccentricity results in higher radiation doses, as the reduced transit time through the outer belt does not compensate for the increased radiation flux from a deeper pass. As a secondary effect of electron penetration in aluminium, Bremsstrahlung shows little contribution to the overall dose and follows the same relationship to orbit geometry as that of trapped electrons. Solar proton dose shows close to no variation from orbit to orbit, with little magnetic shielding variations for such high-altitude orbits. Unlike in LEO, no increased solar particle densities are experienced by inclined orbits passing over the polar regions, agreeing with other research [34]. The reduction in Solar proton TID, which is visible at high eccentricities, can be explained by the shielding effect of the Outer Van Allen Belt. In which the deeper pass through this belt shields the highly eccentric orbit from solar particles. The effect however, is quite limited. The aggregated TID of the Tundra orbit options compare favourably to the yearly 5 krad dose of GEO, with the classical Tundra orbit of 0.2 eccentricity and 63 deg inclination with a 58% lower dose.

A.5 SINGLE EVENT UPSETS

The likelihood of SEU has been assessed by estimating the SEU rates using a default SPENVIS Silicon device under 4mm Aluminium shielding. This analysis incorporates a worst-case scenario of a 5-minute intense particle radiation exposure typical in various orbital environments. The calculation includes contributions from solar particles, trapped protons, and GCR. It is important to note that the device used in this analysis serves as a standard benchmark to identify relative differences across orbital paths rather than providing absolute SEU rates. The difference in SEU in Figure 14 shows little variations over orbits, as was visible in Solar proton TID. The protective geomagnetic shielding effect is only significant for a high inclination orbit of 0.4+ eccentricity.

A.6 DEEP CHARGING

Charging is identified as the root cause of more than 50% of satellite anomalies, necessitating a first-order approximation of its effects. Detailed analysis of charging effects is left for future analysis, requiring detailed knowledge of the spacecraft materials and properties. Deep transits through the electron belt pose a risk of internal deep dielectric charging due to high electron flux intensities. A 'safe' threshold of penetrating radiation has been established at a mean 10h flux of 10^5 *electron/cm²/s* [35]. This threshold is particularly critical for satellites in eccentric orbits, which frequently pass through region of heightened fluence in the outer Van Allen Belt. The penetrating electron flux has been analysed using the

MFLUX tool in SPENVIS, with AE9 electrons at a 95% confidence interval with 1g/cm^2 (3.7mm) aluminium shielding. For a GEO satellite, the reference shielded flux was computed to 1.04e5 $electron/cm^2/s$, slightly above the established safe limit. It was observed that the majority of Tundra orbits exceed this margin considerably. Notably, orbits with a low eccentricity and high inclination benefit from the shorter exposure times within the radiation belt and avoiding passing through higher electron density areas. Subsequent analysis of increased aluminium shield of 2g/cm^2 was able to achieve penetrating fluxes far below the required threshold.

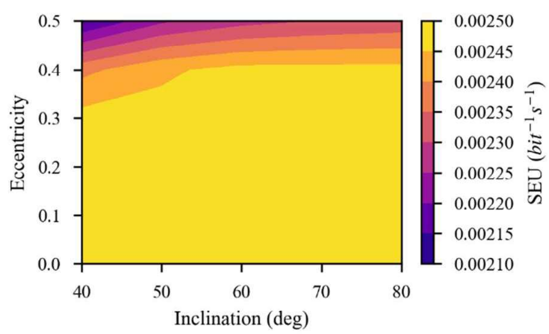

Figure 14: Single Event Upset 5 min worst case.

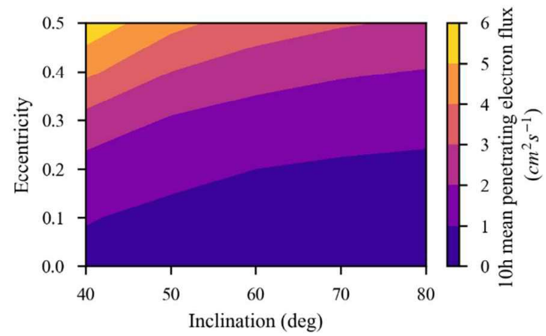

Figure 15: Shielded electron flux, 10hour mean.

A.7 SURFACE CHARGING

Surface charging occurs due to satellite surface interaction with plasma and solar UV; causing the surface to adopt a charge that balances the net current. This interaction varies due to differences in materials, shadows, and plasma conditions, leading to varying surface potentials that may cause electronic discharges into space. Analysing surface charging is highly complex, as it depends on the specific satellite configuration and the surrounding charging environment. Consequently, a qualitative assessment of the trends in the design space of interest is presented here. Equatorial orbits, and GEO specifically, are under the influence of sub-storm plasma injections. The periodic re-connection of the plasma-sphere tail at the Earth's midnight side generates a movement of energised ions and electrons towards Earth. This cloud of electrons circulates westward along Earth's magnetic field lines, reaching geostationary altitudes primarily at the midnight and noon positions and causing the majority of the charging events. Such electron dynamics also apply to highly elliptical orbits, which intersect the geosynchronous altitude magnetic field line between 00:00 and 06:00h, as documented by Fennell [36]. This evidence suggests that Tundra orbits, traversing similar altitude, are likely to experience comparable charging events.

A.8 DISCUSSION

In conclusion, a comprehensive examination of environmental effects on Geosynchronous satellites has highlighted the similarities and differences between Tundra and GEO orbits. Notably, Tundra orbits demonstrate a significant mean reduction of 40% in Total Ionization Dose compared to GEO. However, a pronounced vulnerability to deep electric charging is observed in Tundra orbits with eccentricities exceeding 0.2, attributed to more frequent and deeper passes through the electron belt. Noting however that increased shielding effectively mitigates low energy electron penetration. Magnetic shielding effects appear to have minimal impact, with only negligible variation in solar proton dose and particle induced SEU rates (+-5%). Nevertheless, there is a marginal reduction in SEU rates at higher eccentricities, although these orbits are less favourable due to increased risks associated with deep charging. While surface charging effects have not been explicitly analysed in this study, insights from measurements in highly elliptical orbits suggest that the environment in Tundra orbits would resemble closely to that of sub storm charging events in GEO. From our findings a significant number of inclined and moderately eccentric Tundra orbits demonstrate environmental performance that is comparable, if not superior, to that of GEO orbits. The reduced TID in these orbits potentially allows for the downsizing of solar arrays, as less robust shielding against radiation damage and charging may be required, thus impacting both the cost and weight of future VHTS.

REFERENCES

[1] Vardan Semerjyan et al., "Optical feeder links for GEO satellites at Viasat Inc.," *Free-Space Laser Communications*, vol. 12877, no. XXXVI, pp. 510-521, 2024.

[2] Sylvain Poulenard, Michael Crosnier, and Angélique Rissons , "Ground segment design for broadband geostationary satellite with optical feeder link," *Journal of Optical Communications and Networking*, vol. 7, no. 4, pp. 325-336, 2015.

[3] Amar Mody and Eva Gonzalez, "An operator's view: The medium-term feasibility of an optical feeder link for VHTS," in *2017 IEEE International Conference on Space Optical Systems and Applications (ICSOS)*, 2017, pp. 278-285.

[4] Dirk Gigenbach, Erich Lutz, Juraj Poliak, Ramon Mata-Calvo, and Christian Fuchs, "A high-throughput satellite system for serving whole europe with fast internet service, employing optical feeder links," in *Broadband Coverage in Germany 9th ITG Symposium.*, 2015, pp. 1-7.

[5] Nicolas Perlot, Thomas Dreischer, Carl M Weinert, and Josep Perdigues, "Optical GEO feeder link design," in *2012 Future Network & Mobile Summit (FutureNetw)*, 2012, pp. 1-8.

[6] H Bischl et al., "Feasibility assessment of optical technologies and techniques for reliable high capacity feeder links," ESA, Technical report 21991/09/NL/US, 2010.

[7] Dirk Giggenbach and Amita Shrestha, "Atmospheric absorption and scattering impact on optical satellite-ground links," *International Journal of Satellite Communications and Networking*, vol. 40, no. 2, pp. 157-176, 2022.

[8] Hamid Hemmati, *Near-Earth Laser Communications*.: CRC press, 2020, ch. 1.

[9] Stijn Mast, Lucien Canuet, Thai-Chien Bui, and Thomas Dreischer, "Tundra satellite orbits for very high-throughput optical feederlinks – Part I: mission geometry and coherent intradyne communications," in *International Conference on Space Optics – ICSO 2024*, 2024, [Manuscript submitted for publication].

[10] Consultative Committee for Space Data Systems, "Real-Time Weather and Atmospheric Characterization Data," nformational Report, Green Book CCSDS 140.1-G-2, 2024.

[11] Dirk Giggenbach, "Optimierung der optischen freiraumkommunikation durch die turbulente atmosphäre-focal array receiver," Institute of Communication and Navigation, Digital Networks, PhD thesis 2005.

[12] Donald L Walters and William L Bradford, "Measurements of r0 and t0: two decades and 18 sites," *Applied optics*, vol. 36, no. 300, pp. 7876-7886, 1997.

[13] DL Walters, DL Favier, and JR Hines, "Vertical path atmospheric MTF measurements," *JOSA*, vol. 669, no. 6, pp. 828-837, 1979.

[14] Thang V Nguyen, Hoang D Le, Tanh V Pham, and Anh T Pham, "Link availability of satellite-based FSO communications in the presence of clouds and turbulence," *IEICE Communications Express*, vol. 10, no. 5, pp. 206-211, 2021.

[15] Héctor Vázquez Ramió et al., "European extremely large telescope site characterization. II. High angular resolution parameters," *Publications of the Astronomical Society of the Pacific*, vol. 124, no. 918, 2012.

[16] Yukun Wang et al., "Performance analysis of an adaptive optics system for free-space optics communication through atmospheric turbulence," *Scientific reports*, vol. 8, no. 1, p. 1124, 2018.

[17] Klaus Kudielka, Edgar Fischer, Thomas Berkefeld, and Christoph Fischer, "Optical feeder link demonstrations between the ESA Optical Ground Station and Alphasat," in *2023 IEEE International Conference on Space Optical Systems and Applications (ICSOS)*, 2023, pp. 64-68.

[18] Hongtao Zhang, FuChang Yin, Bing Xu, and Wenhan Jiang, "Low-order mode correction anisoplanatism limitations for adaptive optics system," *Optical Engineering*, vol. 42, no. 8, pp. 2190-2196, 2003.

[19] Ronald Parenti, Richard J Sasiel, Larry C Andrews, and Ronald L Phillips, "Modeling the PDF for the irradiance of an uplink beam in the presence of beam wander," in *Atmospheric Propagation III*, vol. 6215, 2006, pp. 42-54.

[20] Richard J Sasiela, *Electromagnetic wave propagation in turbulence: evaluation and application of Mellin transforms*.: Springer Science & Business Media, 2012, vol. 18.

[21] Larry C Andrews, Ronald L Phillips, Richard J Sasiela, and Ronald Parenti, "PDF models for uplink to space in the presence of beam wander," in *Atmospheric Propagation IV*, vol. 6551, 2007, pp. 92-103.

[22] John W Hardy, *Adaptive optics for astronomical telescopes*, 16th ed. USA: Oxford University Press, 1998.

[23] David Alaluf and Perdigues J M Armengol, "Ground-to-satellite optical links: how effective is an uplink Tip/Tilt pre-compensation based on the satellite signal?," *CEAS Space Journal*, pp. 1-12, 2021.

[24] Stephane Gagnon et al., "Recent developments in satellite laser communications: Canadian context," in *Proceedings of 2012 International Conference on Space Optical Systems and Applications*, 2012, pp. 9-12.

[25] Canadian Radio-television and Telecommunications Commission. (2023) Broadband fund map of areas that are eligible for funding under the broadband fund. [Online]. https://crtc.gc.ca/eng/internet/map-carte.htm

[26] Elena Fantino, R M Flores, Marilena Di Carlo, Alessio Di Salvo, and E Cabot, "Geosynchronous inclined orbits for high-latitude communications," *Acta astronautica*, vol. 140, pp. 570-582, 2017.

[27] D Heynderickx, B Quaghebeur, J Wera, E J Daly, and H D R Evans, "New radiation environment and effects models in the European Space Agency's Space Environment Information System (SPENVIS)," *Space Weather*, vol. 2, no. 10, 2004.

[28] L D Trichtchenko, L V Nikitina, A P Trishchenko, and L Garand, "Highly elliptical orbits for arctic observations: Assessment of ionizing radiation," *Advances in Space Research*, vol. 54, no. 11, pp. 2398-2414, 2014.

[29] T P O'Brien et al., "Changes in ae9/ap9-irene version 1.5," *IEEE Transactions on Nuclear Science*, vol. 1, no. 65, pp. 462-46, 2017.

[30] Michael Anthony Xapsos, J L Barth, E G Stassinopoulos, Edward A Burke, and G B Gee, "Space environment effects: Model for emission of solar protons (ESP): Cumulative and worst case event fluences," Goddard Space Flight Center , 20000021506, 1999.

[31] M A Xapsos, C Stauffer, T Jordan, J L Barth, and R A Mewaldt, "Model for cumulative solar heavy ion energy and linear energy transfer spectra," *IEE Transactions on Nuclear Science*, vol. 54, no. 6, pp. 1985-1989, 2007.

[32] Allan J Tylkan et al., "CREME96: A revision of the cosmic ray effects on micro-electronics code," *IEEE Transactions on Nuclear Science*, vol. 44, no. 6, pp. 2150-2160, 1997.

[33] Stephen M Seltzer, "Updated calculations for routine space-shielding radiation dose estimates: SHIELDOSE-2," United States Environmental Protection Agency, NTIS/02999233_a , 1994.

[34] Wayan Suparta and Siti Katrina Zulkeple, "Spatial analysis of galactic cosmic ray particles in low earth orbit/near equator orbit using SPENVIS," in *Journal of Physics: Conference Series*, 2014.

[35] Joseph F Fennell, Harru C Koons, Margaret W Chen, and Bernard J Blake, "Internal charging: A preliminary environmental specification for satellites," *IEEE transactions on plasma science*, vol. 28, no. 6, pp. 2029-2036, 2000.

[36] Joseph F Fennell, H C Koons, J L Roeder, and J B Blake, "Spacecraft charging: Observations and relationship to satellite anomalies," in *Spacecraft Charging Technology, Proceedings of the Seventh International Conference*, vol. 476, 2001, p. 279.

[37] Geoge C Valley, "Isoplanatic degradation of tilt correction and short-term imaging systems," *Applied Optics*, vol. 19, no. 4, pp. 574-577, 1980.

[38] "Zernike polynomials and atmospheric turbulence".

[39] Robert J Noll, "Zernike polynomials and atmospheric turbulence," *JOsA*, vol. 66, no. 3, pp. 207-211, 1976.

[40] George C Valley, "Isoplanatic degradation of tilt correction and short-term imaging systems," *Applied Optics*, vol. 19, no. 4, pp. 574-577, 1980.